Single-cell transcriptomics reveals cellular hierarchies and aberrant CTS contraction-mediated premature hair regression in androgenetic alopecia

Guo Li[1, 2, 3, 4, #], Li Yang[1, 2, 3, 4, #], Shixin Duan[1, 2, 3, 4], Mengting Chen[1, 2, 3, 4], Yujin Zhang[5], Fangfen Liu[1, 2, 3, 4], Yan Tang[1, 2, 3, 4], Yunying Wang[1, 2, 3, 4, 6], Jiayun Li[1, 2, 3, 4], San Xu[1, 2, 3, 4], Zheng Wu[1, 2, 3, 4], Ben Wang[1, 2, 3, 4], Zhixiang Zhao[1, 2, 3, 4], Wei Shi[1, 2, 3, 4], Hongfu Xie[1, 2, 3, 4], Zhili Deng[1, 2, 3, 4, *], Ji Li[1 ,2, 3, 4, *]

[1]Department of Dermatology, Xiangya Hospital, Central South University, Changsha, Hunan, China.

[2]Hunan Key Laboratory of Aging Biology, Xiangya Hospital, Central South University, Changsha, Hunan, China.

[3]National Clinical Research Center for Geriatric Disorders, Xiangya Hospital, Central South University, Changsha, Hunan, China.

[4]FuRong Laboratory, Changsha, China

[5]Department of Dermatology, The Second Hospital of Hunan University of Chinese Medicine, Changsha, Hunan, China.

[6]Department of Dermatology, Second Affiliated Hospital of Xinjiang Medical University, Urumqi, China.

[#]These authors contributed equally: Guo Li, Li Yang.

[*]Corresponding authors: Ji Li, E-mail: liji_xy@csu.edu.cn; Zhili Deng, E-mail: dengzhili@csu.edu.cn.

Abstract

Androgenetic alopecia (AGA) is characterized by progressive miniaturization of hair, forming a distinctive patterned baldness in the scalp; yet, the mechanisms for hair miniaturization in this disease remain largely unknown. Here by single-cell transcriptome analysis, we describe a concise single-cell atlas, and identify the early changes in cell subpopulations, hair follicle (HF) stem cell fate determination and cell-cell communications in AGA anagen HF units. Thereinto, apoptotic loss of HF progenitor cells is significantly increased, correlated with HF miniaturization in AGA. Mechanistically, enhanced contraction of connective tissue sheath (CTS) activates the mechanosensitive channel PIEZO1, which triggers ectopic apoptosis of progenitor cells in human anagen HFs. Continuous CTS contraction during AGA causes long-term loss of progenitor cells via inducing persistent ectopic apoptosis through PIEZO1, eventually leading to premature hair regression. Most importantly, we show that targeting CTS contraction by ML-7, a selective myosin light chain kinase (MLCK) inhibitor, can obviously improve the growth of HFs from balding scalps of AGA patients. Our study reveals the cellular hierarchies and identifies CTS with increased muscle contraction activity as a driver of premature hair regression in AGA, highlighting CTS surrounding human HF as the therapeutic target for treating this disorder.

Introduction

Androgenetic alopecia (AGA), also known as male pattern baldness, is the most common type of baldness, affecting both men and women. Testosterone and androgen receptor (AR) signaling pathway are considered to be necessary for AGA development(*1, 2*). Genetic susceptibility loci mapping to AR gene and its neighboring ectodysplasin A2 receptor gene (EDA2R) have also been found in AGA(*3*). Current recognized therapies for AGA include finasteride, minoxidil, platelet-rich plasma (PRP) and low-level laser light therapy (LLLT)(*4, 5*). Among these, finasteride suppresses the activity of 5-a reductase 2 (SRD5A2), which transforms testosterone to dihydrotestosterone (DHT), a more potent AR

agonist(*1*). Although the potential targets of other therapies remain elusive, additional factors are suggested to be involved in the development of AGA besides AR-related pathways; however, specific instances have not been conclusively identified.

AGA is featured by the progressive and patterned conversion of large terminal hair follicles (HFs) into small vellus HFs (termed as HF miniaturization), which eventually results in balding(*6*). All HFs undergo periodic cycles of growth (anagen), regression (catagen), and rest (telogen) stages throughout the lifetime(*7*). Normally, most human hair follicles will remain in anagen for 2-6 years to produce large terminal hair. But in AGA, the growth phase decreases to only days or weeks, followed by premature entry into hair regression; this leads to an increase in the percentage of resting HFs, generating microscopic hairs in the balding scalp as the HF cycles(*8, 9*). In HF cycle, the growth of HFs relies on the proliferation and differentiation of HF stem/progenitor cells, whose activities are mainly regulated by the components of HF niche (including dermal papilla (DP), dermal sheath (DS), adipocytes and blood vessels *etc*.)(*6, 10-13*). In balding scalp of AGA, HF stem cells (HFSCs), also known as bulge cells, are basically retained, whereas the number of progenitor cells, a cluster of more actively proliferating cells, is decreased(*14*). This suggests that HFs in AGA balding scalp lack fuels for growth, but the details and underlying mechanism are unclear.

To date, the pathogenetic study of AGA has been scant and limited to histomorphology, global gene analysis and immunohistochemistry due to the fact that most laboratory models are not fully representive of AGA(*15, 16*). Single-cell RNA-sequencing (scRNA-seq) has emerged as a powerful tool for dissecting the transcriptome dynamics, cell heterogeneity, cell lineage tracing and cell-cell communications in complex tissues at uniquely high resolution(*17-21*). However, to our knowledge, a study regarding scRNA-seq application for exploring the pathogenesis of AGA has never been described.

In this study, we report a comprehensive scRNA-seq analysis on human

89 anagen HF units from 3 conditions: balding frontal and non-balding occipital
90 scalps of patients with AGA, and normal frontal scalps of healthy individuals.
91 With these data, we generated a concise single-cell atlas and elucidated the
92 early cellular and molecular changes in AGA anagen HF units. Importantly, via
93 combining human HF organ culture system, we revealed an essential role of
94 connective tissue sheath (CTS), the analogous structure of murine DS in
95 human, in regulating HF progenitor cell survival in the development of AGA. In
96 AGA, CTS contraction is significantly enhanced, resulting in mechanical
97 compression of HF progenitor cells; increased mechanical force activates the
98 mechanosensitive calcium channel PIEZO1, thus induces apoptotic loss of
99 progenitor cells, which eventually leads to premature hair regression. Finally,
100 we demonstrated that targeting CTS contraction by ML-7 can promote the
101 growth of HFs from the balding scalps of AGA patients, even better than
102 minoxidil. These findings illustrate the cellular hierarchies in AGA and
103 emphasize relaxing hair follicle by targeting CTS as a promising strategy for its
104 treatment.
105

106 **Results**

107 ***Single-cell RNA-seq reveals cell heterogeneity of androgenetic alopecia***
108 ***and healthy anagen HF units***

109 To dissect the cellular heterogeneity and explore the early changes in AGA
110 development, we obtained anagen HFs from frontal balding (B) scalps and
111 occipital non-balding (NB) scalps of AGA patients, and frontal normal scalps of
112 healthy individuals (HS), to perform scRNA-seq (Fig. 1A). Among these,
113 anagen HFs of balding scalps were at the early stage of hair miniaturization,
114 isolated from the edge of frontal hairline of AGA patients. First, to identify the
115 hair cycle phase of human HFs, we established an identification strategy by
116 integrating multiple methods reported previously(*22, 23*) (Fig. S1). Before
117 conducting scRNA-seq, the HFs were confirmed in anagen phase. After
118 sequencing and stringent cell filtration, 76368 cells were retained for

subsequent analyses. Following a standard scRNA-seq data analysis procedure, totally 28 clusters (C0-C27) were retained, which were sufficiently separated from each other (Fig. S2A), and these clusters could be reproduced using cells from each of the 12 samples, suggesting that they are robustly present across different samples and conditions (including HS, NB and B) (Fig. S2B, C).

To dissect the cell types, we first defined the expression pattern of SOX9 (Fig. S2D), a reported marker for hair follicle cells(*24*). By immunohistochemistry, we confirmed that SOX9 is expressed in most cells of hair follicle and almost none in other cells, distinguishing hair follicle cells from other epidermal and dermal cells (Fig. S2E). Based on the expression of SOX9, the above clusters were further identified as 20 different cell types, according to the expression of known lineage markers, including Bulge (KRT15$^+$, CXCL14$^+$), DP (VCAN$^+$, CFD$^+$), DS (ACTA2$^+$, CCN2$^+$), outer root sheat basal (ORS, KRT14$^+$, PTHLH$^+$), ORS suprabasal (ORS SB, KRT17$^+$), inner root sheat (KRT6A$^+$), medulla (KRT85$^+$, KRT31$^+$), proliferating progenitors (PR, MKI67$^+$), endothelial cells (Endo, PECAM1$^+$, VWF$^+$), immune cells (CD3D$^+$), Langerhans (CD207$^+$, CD1A$^+$), Melanocytes (DCT$^+$, MLANA$^+$), Vascular smooth muscle cells/pericytes (vSMC, ACTA2$^+$, RGS5$^+$, RERGL$^+$), Sebaceous gland cells (DCD$^+$, SCD$^+$), sweet gland cells (SwG, KRT8$^+$, KRT18$^+$), interfollicular epidermis spinous (IFE spinous, KRT1$^+$, KRT10$^+$), IFE granular (FLG$^+$, KRT2$^+$); cells highly expressing KRT14 but not SOX9 were defined as IFE basal; Inner II (KRT79$^+$) is the outer layer of Infundibulum and Isthmus which highly expressed KRT14 and KRT6A in the upper HF region; in contrast, Outer II has a relatively low expression of KRT6A(*25-35*) (Fig. 1B-D; Supplementary Table 1; Fig. S2F-K).

To investigate the trajectories among all 20 cell types, monocle3(*36*) was employed to perform the pseudotime analysis with the root node setting at start point of bulge on the SOX9$^+$ HF branch and start point of IFE basal on the SOX9$^-$ IFE branch separately. Our data demonstrate that bulge cells first differentiate into ORS and IRS cells, which then further branch into SOX9$^+$ PR,

149 also known as matrix cells, and finally contribute to medulla (HF) formation. For
150 the SOX9$^-$ IFE branch, IFE basal cells can directly differentiate into SOX9$^-$ PR
151 and IFE spinous cells which finally develop into IFE granular cells (Fig. 1E).
152 These patterns are consistent with the knowledge from previous studies(*26, 35*).
153 Consistent with the scRNA-seq data, immunostaining analysis showed that
154 KRT15 was highly expressed in bulge HFSCs and moderately expressed in IFE
155 basal cells (Fig.1F), similar to previous observations(*14, 26*). As an IRS marker,
156 KRT6A was exactly expressed mainly in the IRS and some of the inner layer
157 cells of the infundibulum and isthmus, which are the upward continuation of IRS
158 (Fig.1G and Fig. S2L). Moreover, we verified IFE spinous cells with KRT10 and
159 DS cells with α-SMA (Fig. 1H, I). We determined the relative proportion of each
160 cell type in all samples, showing increased DS and sebaceous gland cells in B
161 anagen HF units compared with NB or HS (Fig. S2M). We next explored the
162 number of differentially expressed genes (DEGs) between B and NB/HS. The
163 results showed that all cell types had differences in various degree (Fig. S2N,
164 Supplementary Table 2), suggesting that anagen HFs undergo significant
165 changes at the early stage of hair miniaturization in AGA.
166 To further explore the potential heterogeneity, bulge cells were subclustered
167 into three distinct subclusters (Fig. 2A), in which the percentage of subcluster
168 1 was reduced in the balding bulge of AGA patients (Fig. 2B). Wilcoxon rank-
169 sum test was used to characterize the marker genes specifically enriched in
170 each subpopulation versus other subpopulations. Top marker genes with
171 avg_log2FC>0.25, pct (minimum fraction in either of the two populations)>0.25
172 and P value<0.05 of each subcluster were showed in Fig. S3A and
173 Supplementary Table 3. Among these, KRT15 was commonly highly expressed
174 (Fig. 2C); CD200 was visibly enriched in subcluster 0 (Fig. 2D), while CD34
175 was mainly enriched in subcluster 1 (Fig. 2E). Consistently, CD34$^+$ bulge cells
176 were decreased in the bulge of balding anagen HFs (Fig. 2F). By
177 immunostaining, we defined that CD200$^+$ cells are located in the upper bulge
178 with high stemness (known as HFSCs), while CD34 is mainly expressed in the

179 lower bulge cells referred to as HF progenitor cells, which are differentiated
180 from the upper bulge HFSCs (Fig. 2G, H). Via RNA Velocyto analysis, we further
181 confirmed that CD200$^+$ bulge cells are the HFSCs, which have the ability to
182 differentiate into CD34$^+$ progenitor cells (Fig. 2I).

183 PR cells are the proliferating progenitors which highly expressed MKI67.
184 Further subclustering analysis separated PR cells into 2 subclusters (Fig. S3B).
185 Cell composition analysis showed the subcluster 1 decreased in B anagen HFs
186 of AGA (Fig. S3C). Among these two subclusters, one was enriched for
187 epithelial markers (KRT1 and KRT10), representing the IFE proliferating
188 progenitor (ePR) cells; another one (subcluster 1) was specifically enriched for
189 HF cell marker SOX9, suggesting that it represented the HF proliferating
190 progenitors also named as matrix cells (Fig. S3D, E, and Supplementary Table
191 4).

192 Subclustering of DP cells, the signaling center for hair growth(*11*), revealed
193 5 subclusters (Fig. 2J, Fig. S3F and Supplementary Table 5). The percentage
194 and distribution of subclusters were comparable across HS, NB and B,
195 suggesting that DP cell identity may not alter in AGA anagen HFs (Fig. 2K and
196 Supplementary Table 6). Gene ontology (GO) analysis showed that
197 angiogenesis-related pathway was downregulated (Fig. 2L), consistent with our
198 previous findings from bulk RNA sequencing(*6*).

199 DS cells were divided into 4 subclusters (Fig. 2M, Fig. S3G and
200 Supplementary Table 7), which showed no significant changes in the balding
201 anagen HFs of AGA patients (Fig. 2N and Supplementary Table 8). Pathway
202 enrichment analysis of differential genes revealed muscle contraction was
203 obviously upregulated in balding anagen HFs compared to non-balding or
204 healthy groups (Fig. 2O).

205 In human hair follicle, the DS is tightly surrounded by a network of blood
206 vessels, composed of vSMCs and endothelial cells(*37*). Among them, vSMCs
207 were separated into 4 subclusters, and the percentage and distribution of
208 subclusters were comparable across three groups (Fig. 2P, Q; Fig. S3H;

209 Supplementary Table 9 and Supplementary Table 10). Pathway enrichment
210 analysis showed that smooth muscle contraction and multiple pathways
211 involved in inflammatory regulation (such as IL-17 signaling pathway) were
212 upregulated in vSMCs of balding anagen HFs (Fig. 2R). Endothelial cells were
213 divided into 4 subclusters, which exhibited no obvious alterations (Fig. S3I-K;
214 Supplementary Table 11 and Supplementary Table 12), and IL-17 signaling
215 pathway was also upregulated in endothelial cells of balding anagen HFs (Fig.
216 S3L).

217 Immune cells expressing CD3D were further separated into 6 subclusters,
218 including Th17 cells (IL17A$^+$, IL17F$^+$ and IL22$^+$), naive CD4$^+$ T cells (IL7R$^+$),
219 CD8$^+$ T cells (GZMK$^+$ and CD8A$^+$), natural killer T (NKT) cells (ZNF683$^+$) and
220 two unknown subclusters (Fig. S3M-O; Supplementary Table 13). Cell
221 composition analysis showed significant increase of Th17 cells in balding HF
222 units (Fig. S3P, Q), which provides evidence for inflammatory infiltration in AGA.

223 ***Identification of early changes in HFSC fate determination and cell-cell***
224 ***communications in AGA***

225 Epidermal and sebaceous differentiation of HFSCs has been reported to be
226 associated with HF miniaturization during ageing-induced and obesity-induced
227 hair loss in mice(*38, 39*), but it was unclear whether there existed HFSC fate
228 determination alterations in AGA development. To address this question, we
229 conducted cell fate analysis among potential cell types: bulge, ORS, sebaceous
230 gland and IFE basal cells. As expected, more HFSCs showed a
231 pronounced tendency to differentiate into sebaceous gland and IFE basal cells
232 in balding HFs compared with non-balding and healthy HFs, and obviously
233 decreased HFSCs differentiated into ORS cells (Fig. S4A, D). To explore the
234 underlying mechanisms, branched expression analysis modeling (BAEM) was
235 performed, and identified three common cell fate determination genes,
236 COL17A1, PPP1R1C and SGK1 (Fig. S4B, C, E, F).

237 To further characterize the cell-cell communications between different cell
238 types in HF units. Cellchat(*21*) was employed to compare the cell-cell

239 communications between balding and non-balding/healthy HFs. Although the
240 interaction strength showed that most cell types had no obvious changes in
241 incoming and outgoing interaction strength, Th17 cells and langerhans
242 exhibited increased incoming interaction strength in balding and non-balding
243 HFs compared to healthy HFs, while ORS cells displayed decreased outgoing
244 interaction strength in balding anagen HFs in AGA (Fig. S4G).

245 ***Apoptotic loss of HF progenitor cells is correlated with HF miniaturization***
246 ***in AGA***

247 AGA is characterized by the progressive conversion of the terminal (t) scalp
248 HFs into intermediate/miniaturized (i/m) HFs, which we called the process of
249 HF miniaturization and may be attributed to the deficiency of progenitor cells
250 based on our scRNA-seq data as mentioned above and the early study(*14*). To
251 verify changes in HFSC and progenitor cell numbers, we performed
252 immunostaining of CD200 and CD34 on anagen HFs from frontal balding (B)
253 and occipital non-balding scalps (NB) of AGA patients, and frontal normal
254 scalps of healthy individuals (HS). HFs retain $CD200^+$ HFSCs with the same
255 percentage in AGA, despite a decrease in cell numbers in B scalps (Fig. S5A-
256 C). However, $CD34^+$ progenitor cells were gradually diminished during the
257 process of HF miniaturization (Fig. 3A-C). Further analysis indicated a strong
258 positive correlation between the number/ proportion of $CD34^+$ progenitor cells
259 and the hair follicle diameter in balding scalps of AGA patients (Fig. 3D-G).
260 Collectively, these observations suggest that loss of progenitor cells is
261 associated with HF miniaturization in AGA.

262 Next, investigation into the causes of the progenitor cell loss via signaling
263 pathway enrichment analysis revealed upregulated apoptotic signals in
264 progenitor cells of balding anagen HFs (Fig. 3H). A significant increase in
265 apoptosis was observed in the $CD34^+$ progenitor cells of balding anagen HFs
266 according to Cleaved Caspase-3 staining (Fig. 3I, J). These results support the
267 notion that an apoptosis-induced gradual loss of $CD34^+$ progenitor cells may be
268 involved in the HF miniaturization in AGA.

Hyperactive CTS contraction drives premature hair regression via inducing apoptosis of progenitor cells in AGA

Intimate crosstalk between stem cells and the surrounding microenvironment is vital for stem cell fate decisions. On the outside of the progenitor cells is a layer of elastic DS in murine pelage HF, while in human scalp HF is the multi-layer of connective tissue sheath (CTS) mainly composed of DS cells, collagens and vasculature (including vSMCs and endothelial cells) (*37*)(Fig. S6A; Fig. 4A, B). Pathway enrichment analysis revealed increased contractile activity in both DS cells and vSMCs of balding anagen HFs compared to non-balding or healthy groups (Fig. 2O and R), which can be confirmed by the immunostaining of phosphorylated myosin light chain 2 (p-MLC2), a marker of myosin active state(*40*) (Fig. 4C, D; Fig. S6B, C). Collectively, these results suggest that CTS contraction is enhanced in anagen HFs of balding scalps in AGA patients.

Given that the contractile force of DS is a key driver of HF regression during hair regeneration in mice(*12*), we wondered whether excessive contraction of the progenitor cell-encapsulating CTS, the analogous structure of murine DS in human, might affect hair follicle by modulating progenitor cell fate in AGA. To this end, we utilized methacholine (MCH)(*41, 42*) and norepinephrine (NE)(*43, 44*) to activate CTS contraction in the in vitro cultured human anagen HF organs. The efficiency of MCH and NE on contraction activation in this model was evaluated and verified by p-MLC2 immunostaining (Fig. S6D). Strikingly, HF growth was significantly inhibited (Fig. S6E-G) and premature catagen induction was promoted (Fig. S6H, I) in normal anagen HFs treated with MCH or NE. Furthermore, the observed activation of CTS contraction by MCH resulted in a dose-dependent negative effect on hair growth and anagen maintenance (Fig. 4E-H, and Fig. S7A, B). To figure out whether progenitor cells act as the targets of CTS contraction, we examined the effect of MCH on the number and apoptosis of HF progenitor cells. The immunostaining of CD34 and Cleaved Caspase-3 showed that activated CTS contraction by MCH promoted the loss and apoptosis of $CD34^+$ progenitor cells in a concentration-dependent

299 manner. Of note, Cleaved Caspase-3^{+}CD34^{+} cells are barely detectable under
300 100 μM MCH treatment due to the fact that CD34^{+} progenitor cells were almost
301 depleted under this condition (Fig. 4I-L).

302 Notably, blockade of CTS contraction with ML-7 (Fig. S7C), a specific myosin
303 activation inhibitor(*45*), not only improved the growth retardation and catagen
304 premature induction (Fig. 4M-O, and Fig. S7D), but also restored the apoptotic
305 loss of progenitor cells in MCH-treated human HFs (Fig. 4P-S), confirming the
306 critical role of CTS contraction in MCH effects. Consistently, we demonstrated
307 that the percentage of catagen HFs is indeed markedly increased in the B
308 scalps of AGA patients compared to NB or HS scalps (Fig. 4T-V). Collectively,
309 these findings significantly strengthen the link between enhanced CTS
310 contraction and AGA pathogenesis.

311 Subsequently, to determine whether apoptosis is necessary, we applied Z-
312 VAD-FMK to block cell apoptosis(*46*). Our results showed that the observed
313 phenotypes caused by MCH, including HF growth inhibition (Fig. 5A-D),
314 premature catagen induction (Fig. 5E) and depletion of CD34^{+} progenitor cells
315 (Fig. 5F-I), were counteracted after Z-VAD-FMK administration. Taken together,
316 these data suggest that over-activated CTS contraction compresses hair
317 growth and drives premature hair regression via promoting the apoptosis of
318 progenitor cells.

319 ***CTS contraction induces progenitor cell apoptosis and premature hair***
320 ***regression via PIEZO1 signaling in AGA***

321 To pinpoint the specific molecular mechanisms by which the contractility of CTS
322 regulates progenitor cells, we first examined the expression levels of the known
323 mechanosensitive ion channel protein PIEZO1, which has been found to be
324 highly expressed in HFSCs in mice(*47*). Our results showed that PIEZO1 was
325 abundantly expressed in CD34^{+} progenitor cells (Fig. S8A) and was expressed
326 at much higher levels in balding anagen HFs compared to non-balding group
327 (Fig. 6A, B). We then used intracellular Ca^{2+} as a downstream indicator of
328 PIEZO1 signaling(*48, 49*). As quantified by Fluo-4 (a Calcium influx indicator)

329 RFI, there was a significant increase in intracellular Ca^{2+} concentration in
330 $CD34^{+}$ progenitor cells of balding anagen HFs (Fig. 6C, D). These results
331 suggest that PIEZO1 signaling is activated in progenitor cells of balding anagen
332 HFs.

333 We next investigated whether activation of PIEZO1 is sufficient to induce HF
334 growth retardation and premature regression. To this end, we applied YODA1,
335 a PIEZO1-specific activator to cultured anagen HFs (Fig. S8B, C). Intriguingly,
336 anagen HFs treated with YODA1 displayed a phenotype similar to MCH (Fig.
337 6E-K and Fig. S8D). In addition, the Ca^{2+} concentration in MCH-treated HF
338 progenitor cells was elevated and could be reversed by the specific PIEZO1
339 inhibitor GsMTX4 and the myosin activation inhibitor ML-7 (Fig. 6L, M),
340 indicating the activation of PIEZO1 signaling by CTS contraction. Not
341 surprisingly, inhibition of PIEZO1 signaling by GsMTX4 rescued the phenotypes
342 induced by MCH (Fig. 6N-T and Fig. S8E).

343 These results prompt us to speculate that CTS contraction induced in balding
344 anagen HFs activates the PIEZO1 signaling pathway in progenitor cells via
345 mechano-transduction, thereby inducing progenitor cell apoptosis and thus
346 promoting premature HF regression.

347 ***Targeting CTS contraction by ML-7 improves the growth of HFs from the***
348 ***balding scalps of AGA patients***

349 All the above results inspired us to wonder whether targeting CTS contraction
350 is a promising therapy for AGA. We first obtained anagen HFs from the balding
351 scalps of AGA patients, which had been experiencing the process of
352 miniaturization. As expected, the balding anagen HFs exhibited slower growth
353 compared with those from occipital non-balding scalps of the same AGA
354 patients in ex vivo organ culture system (Fig. S9A-C). We then treated the
355 balding HFs with ML-7, or minoxidil (MNX), the FDA-approved drug for AGA
356 treatment. Immunostaining of p-MLC2 confirmed that ML-7 abolished muscle
357 contraction activity in CTS, but MNX did not (Fig. S9D). Excitingly, ML-7 could
358 significantly improve the growth and premature regression of balding HFs of

359 AGA patients, even better than MNX (Fig. 7A-D; Fig. S9E). Consistently, ML-7
360 showed a better effect on decreasing the apoptotic loss of progenitor cells
361 compared with MNX (Fig. 7E, F). Furthermore, we demonstrated ML-7 did not
362 affect the growth and anagen-to-catagen progression of cultured anagen HFs
363 from occipital non-balding scalps of AGA patients, suggesting a specific
364 therapeutic effect for balding anagen HFs with enhanced CTS contraction (Fig.
365 S9F-H). Taken together, these findings suggest that relaxing HFs via targeting
366 CTS contraction is a hopeful strategy for AGA therapy.
367

368 **Discussion**

369 Here we have presented what is, to the best of our knowledge, the first and
370 currently the only comprehensive single-cell transcriptome profiling of all
371 cell types within HF units from balding and non-balding scalps of AGA patients
372 compared with healthy individuals. Considering that HFs of balding scalps used
373 in the present study were in anagen phase and at the early stage of hair
374 miniaturization, isolated from the edge of frontal hairline of AGA patients, our
375 high-quality data allowed us to illustrate the early changes in cell
376 subpopulations, the HF cell lineage trajectory and cell-cell communications in
377 AGA in unprecedented detail. Our atlas uncovers at least 16 different broad cell
378 types in human HF unit, which are more than those described in previous
379 scRNA-seq studies(*25, 26*). The reason for this obvious difference could be
380 likely attributed to the optimization of human HF single cell isolation by
381 combining mechanical separation with multienzyme digestion. Based on this,
382 we obtained previously undescribed DP cells and major cell types of CTS
383 (including DS, vSMC and endothelial cells) in human HFs, which are reported
384 to be essential for regulating the growth of hair follicles(*12, 37, 50*). Delineation
385 of DP and CTS cells at single-cell level provides an opportunity to determine
386 the precise roles of these cells in the pathogenesis of AGA.

387 The hair growth is powered by HFSCs (termed as bulge stem cells) that have
388 the ability to give rise to all epithelial components of the hair follicle(*51*).

389 However, current understanding of the cellular and molecular changes in the
390 bulge in AGA development is limited. Our scRNA-seq data show that bulge
391 stem cells contain two major subclusters: $CD200^+$ bulge stem cells and $CD34^+$
392 progenitor cells. Thereinto, the number and percentage of progenitor cells are
393 significantly decreased in the balding anagen HFs of AGA patients. These
394 results are consistent with the previous study showing that balding scalp in men
395 with AGA retains HFSCs but lacks HF progenitor cells(*14*). Besides, we
396 demonstrate that HFSCs are more likely to differentiate into interfollicular
397 epidermal and sebaceous lineages, rather than HF lineage cells, in the balding
398 scalps, which may be responsible for the progressive hair follicle miniaturization
399 and hair thinning in AGA. Similarly, in the case of ageing- and obesity-induced
400 hair loss in mice, those aberrant fate changes also occur in a fraction of HFSCs,
401 which prefer to undergo epidermal and sebocyte differentiation regulated by
402 COL17A1 proteolysis and inflammatory signals respectively, thereby
403 decreasing the HFSC pool and leading to hair follicle miniaturization in a
404 stepwise manner(*38, 39*). Here, our data also suggest an important role of
405 COL17A1 in the aberrant differentiation of HFSCs in AGA development. During
406 normal hair growth, HF stem/progenitor cells proliferate and differentiate to
407 generate hair matrix cells, which rapidly proliferate to produce the hair shaft of
408 growing hair in the end(*52*). Here, we show that the proliferating matrix cells are
409 also decreased in balding HFs in AGA. It is tempting to speculate that the
410 apoptotic loss of progenitor cells contributes to a decrease in matrix cells, which
411 may cause the premature induction of catagen (namely shortening of anagen),
412 and eventually weakens the generation of terminal hair shaft in AGA
413 development.

414 DP acts as the signaling center to govern the proliferation and differentiation
415 of HF stem/progenitor cells in hair growth(*11, 53*). Our previous study
416 demonstrated that androgen receptor (AR) is upregulated in DP cells, which
417 induce apoptosis of microvascular endothelial cells via paracrine signaling in
418 the DP of balding HFs in AGA(*6*). However, in this study, except for the

419 downregulated angiogenesis, our scRNA-seq analysis identifies no other
420 obvious changes in cell subpopulations and signaling pathways, which may be
421 involved in the regulation of hair growth, in DP cells of balding HFs from AGA
422 patients. The reasons for this discrepancy are currently not clear, and further
423 analysis and experimentation will be required to address this point. Although
424 microinflammation has been commonly reported in AGA(*54-57*), the details
425 remain largely undefined. Here, we identity that T cells are the main
426 lymphocytes in human HF units, and AGA is featured by increased Th17 cells.
427 Although a previous study has identified that progenitor cells are significantly
428 diminished by flow cytometry in the bald scalp of AGA patients(*14*), the details
429 in this aspect are obscure. In this study, we further confirm that $CD34^+$
430 progenitor cells are decreased in the balding anagen HFs in AGA, and
431 determine that these progenitor cells are derived from $CD200^+$ bulge stem cells
432 via scRNA-seq analysis and immunostaining. Importantly, we also find that the
433 reduction in HF progenitor cells is attributed to the increased apoptosis, and the
434 number and percentage of these cells is positively correlated with the hair
435 follicle size in the balding scalp in AGA. These findings suggest a pivotal role
436 for progenitor cell depletion in the pathogenesis of AGA.
437 HF growth is tightly spatiotemporally regulated by the crosstalk between
438 stem/progenitor cells and the microenvironment, mainly the mesenchymal
439 niche(*10*). In addition to DP whose role is well recognized, DS is also an
440 important component of the mesenchymal niche. DS is continuous with
441 the DP and generates an envelope surrounding the hair follicle, whose role has
442 been far less examined than the DP yet may be equivalently important for the
443 regulation of hair growth(*37*). Until recently, DS has been identified as smooth
444 muscle that drives hair follicle regression for reuniting HFSCs and niche to
445 regenerate tissue structure during hair regeneration in mice(*12*). Further study
446 demonstrates that progenitor cell-derived endothelin governs DS contraction in
447 mice(*58*). However, the role of CTS (the analogous structure of murine DS in
448 human), in human hair follicle, especially in hair disorders, remains undefined.

449 In this study, via single-cell sequencing analysis we identify that smooth muscle
450 contraction activity is markedly increased in the major cell types of CTS,
451 including DS and vSMC cells in balding anagen HFs of AGA patients. We further,
452 by co-immunostaining, confirm this conclusion, and demonstrate that muscle
453 contraction-related pathways are hyperactivated in the CTS of balding anagen
454 HFs; In human hair follicle organ culture system, activation of muscle
455 contraction in CTS drives premature hair follicle regression via inducing
456 progenitor cell apoptosis. Surprisingly, we find that pharmacological inhibition
457 of muscle contraction can obviously improve the growth and premature catagen
458 induction of hair follicles from the balding scalps of AGA patients, even better
459 than the FDA-approved drug minoxidil, strongly suggesting that targeting
460 muscle contraction in CTS is a very promising therapy for AGA. It will also be
461 interesting in future studies to determine the mechanism that hyperactivates the
462 muscle contraction of CTS cells in the development of AGA.

463 Our results suggest PIEZO1, a mechanosensitive ion channel, as a regulator
464 in HF progenitor cells that senses the mechanical force generated by CTS
465 contraction. We show that PIEZO1 is expressed in HF progenitor cells, and it
466 becomes markedly upregulated and activated in the balding anagen HFs of
467 AGA patients. Inhibition of PIEZO1 signaling evidently alleviates progenitor cell
468 apoptosis and premature hair follicle regression induced by CTS contraction; in
469 contrast, PIEZO1 hyperactivation induces apoptosis of progenitor cells and
470 premature entry into regression in human anagen hair follicles. Similarly,
471 PIEZO1 has been reported to be abundantly expressed in HFSCs, and is
472 responsible for niche-size-decrease-triggered ectopic HFSC apoptosis in
473 mice(*47*). We conclude that the role of PIEZO1 in sensing the abnormal
474 mechanical force from the microenvironment to regulate the HFSC apoptosis is
475 conserved across species, and the mechanosensitive channel might be a
476 therapeutic target for hair loss. However, the detailed molecular mechanisms
477 by which aberrant PIEZO1 activation induces progenitor cell apoptosis in AGA
478 need further study to clarify.

479 In summary, the present study reveals the cellular hierarchies via scRNA-seq
480 analysis and demonstrates hyperactive CTS contraction as a critical cause of
481 hair regression in AGA, strongly suggesting that relaxing hair follicle by
482 targeting CTS might be a promising therapy for this disorder.
483

484 **Methods**

485 **Human scalp and HF samples**

486 Human scalp skin biopsies and HF units were collected from non-balding
487 occipital and balding frontal sites of male AGA patients undergoing hair
488 transplantation surgery, and normal frontal sites of male healthy volunteers from
489 the Department of Dermatology in Xiangya Hospital, Central South University.
490 The procedures were in accordance with protocols set out in the WMA
491 Declaration of Helsinki and the Department of Health and Human Services
492 Belmont Report and approved by the ethical committee of the Xiangya Hospital
493 of Central South University and written informed consent was acquired from all
494 participants.

495 **Identification of hair cycle phases in human HFs**

496 Hair cycle phases of human HFs were determined by morphological analysis,
497 HE staining, co-immunostaining of Ki67 and TUNEL, and immunostaining of
498 Cleaved Caspase-3 (C-Caspase-3) as previously described(*22, 23*). With these
499 identification methods (Fig. S1), all human HFs used in this study (including
500 scRNA-seq, staining and in vitro organ culture) had been confirmed in the
501 typical anagen phase before experimentation unless otherwise stated.

502 **Preparation of single-cell suspensions of HF units**

503 To obtain single-cell suspension of entire HF units, DPs were isolated first by
504 micro-dissection from HFs and were chopped. The remaining hair follicle tissue
505 samples were cut with scissors and digested with the chopped DPs in 4mg/ml
506 Dispase II and Collagenase IV for 40 min at 37℃, centrifuged at 200g for 5min.
507 The pellet was resuspended and digested in 0.25% trypsin for 10 min at 37℃,
508 washed in PBS+5%FBS and filtered through a 70 μm cell strainer. The Dead

509 Cell Removal Kit (Miltenyi Biotec) was used in accordance with the
510 manufacturer's instruction to obtain live cells. 10 μL of the cell suspension were
511 mixed with the same volume of Trypan blue for cell counting. The loading
512 volume for sequencing was verified by the cell concentration

513 **ScRNA-seq**

514 scRNA-seq mainly includes GEM (gel bead-in-emulsion) generation, barcoding,
515 cDNA amplification, library construction and sequencing. These steps were
516 completed according to the user's instructions of Chromium Single Cell 3'
517 Reagent Kits v3.1 (10× Genomics, product code: 1000268, 1000215, 1000120)
518 (https://www.10xgenomics.com/support/single-cell-gene-expression). Libraries
519 were sequenced by an Illumina NovaSeq6000 System. Approximately 10,000
520 cells (targeting 5000–12,000) per sample were used for single-cell RNA
521 sequencing.

522 **ScRNA-seq data processing and cell type identification**

523 We used the default parameters of Cell Ranger software suite (v6.0.2) to align
524 and quantify the raw reads data from 10x Genomics. After the initial Cell Ranger
525 metric assessment, Seurat (v4.3.0)(*59*) in R version 4.3.1 was used to exclude
526 cells with fewer than 200 genes or more than 6000 genes detected, and more
527 than 20% mitochondrial reads for downstream analysis.

528 After quality control, 76368 cells remained and were used for downstream
529 bioinformatic analysis. The "NormalizeData" function was used to normalize the
530 feature expression measurements for each cell by the total expression. The
531 "ScaleData" function was used to scale and center the expression of each gene
532 for dimensional reduction. To avoid batch effects among samples and
533 experiments, we integrated data from all samples using harmony (v0.1.1). Total
534 cell clustering was performed by "FindClusters"function with Louvain algorithm
535 at a resolution of 0.2. Non-linear dimensional reduction was performed by
536 "RunUMAP" function and visualized by Uniform Manifold Approximation and
537 Projection (UMAP). Markers genes of each cell cluster were determined by
538 "FindAllMarkers" function with Wilcoxon rank-sum test. Only those with

539 |‘avg_logFC’| ≥0.25 and ‘adjusted P value’≤0.05 were considered as marker
540 genes.

541 For subgroup cell clustering, cells of each cell type were extracted separately
542 and clustered by their first 20 PCs and appropriate resolution. To further
543 approximate the low-dimensional data manifold representing the differentiation
544 trajectory for Bulge cells, spliced status of mRNAs in single-cell RNA
545 sequencing data were used to estimations of RNA velocities through
546 velocyto(*60*). Markers genes of each subcluster were identified by
547 “FindAllMarkers” function with the default parameters. “DoHeatmap” function
548 were used to show top marker genes in heatmap.

549 **Identification of balding-associated DEGs**

550 We used the function of “FindMakers” in Seurat to identify balding-vs-
551 nonbalding and balding-vs-healthy differentially expressed genes (DEGs) for
552 each cell type and sub-cell type. The adjusted P values of each DEG were
553 calculated by non-parametric two-sided Wilcoxon rank-sum test and only those
554 with |‘avg_logFC’| > 0.25 and ‘adjusted P value’ < 0.05 were considered to be
555 balding-associated DEGs.

556 **Function enrichment analysis**

557 Gene Set Enrichment Analysis (GSEA) of GO and KEGG was performed by
558 clusterProfiler R package (v4.5.1.902) and visualized with ggplot2 R package
559 (v3.4.1)(*61*). Representative terms selected from the top ranked GO terms and
560 KEGG pathways from MsigDB were displayed.

561 **Pseudotime analysis**

562 Monocle3 was used to reconstruct the differentiation trajectory for all cell
563 types(*36*). The expression matrix of all cells was used as input and the UMAP
564 embedding coordinates were import from Seurat result. The start points of
565 bulge and IFE basal cells were specified as the root nodes separately for the
566 $SOX9^{+}$ HF branch and $SOX9^{-}$ IFE branch of the trajectory graph by “order_cells”
567 function. “Plot_cells” function was used to visualize each cell type along the
568 pseudotime trajectory. To further reconstruct the differentiation trajectory and

569 do “branched expression analysis modeling” (BAEM) for bulge cell fate cell
570 determination related cell types, such as bulge to ORS and IFE, Monocle2(*62*)
571 was used to reconstruct the differentiation trajectory for small set of cell types
572 and “BAEM” function were performed to identify cell determination related
573 molecules.

574 **Cell-cell communication analysis**

575 To assess cell-cell communications among different cell types, we used cellchat
576 (v1.1.3) to infer the intercellular communication network from single-cell RNA-
577 seq data. Only cell types with more than 10 cells were considered in the
578 analysis. The “trimean” method is used for calculating the average gene
579 expression per cell group in “computeCommunProb” function. Pairwise
580 comparison and visualization are performed by cellchat build-in function, only
581 interactions with P value lower than 0.05 are considered to be real.

582 **HF organ culture**

583 Human HFs were obtained from the non-balding occipital sites
584 (unless stated otherwise) of male AGA patients undergoing hair transplantation
585 surgery. After microdissection, the HFs were first incubated in William’E
586 medium (WEM, ThermoFisher) for 24 hours to re-equilibrate. HFs in anagen VI
587 phase were randomly assigned to the different experimental groups. HFs were
588 cultured at 37℃ with 5% CO_2 in WEM supplemented with 2 mM of L-glutamine,
589 10 ng/ml hydrocortisone, 10 ug/ml insulin and 1% penicillin/streptomycin mixure,
590 and photographed under a stereoscope every two days to count hair shaft
591 length and hair cycle stage. The hair cycle stage (anagen/early-catagen/mid-
592 catagen) of HFs was determined according to the identification methods
593 described above(*22, 23*).

594 **Chemical stimulation of HFs**

595 All the chemicals were purchased from Selleck. After 24 hours, medium was
596 replaced and HFs were treated with vehicle (0.1% DMSO), MCH (0.1,1 10,100
597 μM as indicated), NE (0.1 μM), ML-7(0.3 μM), Z-VAD-FMK (10 μM), YODA1(15
598 μM), or GsMTX4(1 μM) according to the design of different experiments and

599 the medium was changed daily with the indicated treatment. HFs were cultured
600 for 2-10 days for analysis of hair growth and immunostaining.

601 **Immunostaining and TUNEL staining**

602 Immunostaining was performed as previously described(*63*). Briefly, OCT-
603 embedded samples were sectioned (10 μm) with a Leica cryostat. The sections
604 were fixed for 10 min with 4% PFA, and washed with PBS, then blocked for 60
605 min with blocking buffer (5% NDS, 1% BSA, 0.3% Triton X-100). Primary
606 antibodies were incubated overnight at 4℃. Secondary antibody was incubated
607 for 60 min at room temperature. After washed, sections were counterstained
608 with DAPI. TUENL staining was performed with TUNEL assay kit (Roche, USA)
609 according to manufacturer's instructions, and then stained with CD34 following
610 the immunostaining protocol. For the co-immunostaining of two antibodies from
611 the same host species, double immunohistochemistry for paraffin sections (8
612 μm) was conducted by using the Opal 4 color manual immunohistochemistry
613 (IHC) kit (NEL810001KT, PerkinElmer). The signal of p-MLC2 was amplified by
614 the Opal 4 color manual IHC kit (NEL810001KT, PerkinElmer). All pictures
615 were taken with a Zeiss Axioplan 2 microscope. The fluorescence intensity was
616 evaluated with ImageJ. The primary antibodies were used in this study: Rabbit
617 anti-SOX9 (1:100, Cell Signaling), Mouse anti-KRT15 (1:2000, Lab vision),
618 Mouse anti-KRT14 (1:4000, Abcam), Rabbit anti-KRT6A (1:500, Atlas
619 Antibodies), Rabbit anti-KRT10 (1:1000, Abcam), Mouse anti-α-SMA (1:4000,
620 Abcam), Rabbit anti-CD200 (1:200, Cell Signaling), Rabbit anti-CD34 (1:250,
621 Abcam), Rabbit anti-Cleaved Caspase-3 (1:400, Cell Signaling), Rabbit anti-p-
622 MLC2 (1:100, Cell Signaling), Rabbit anti-Ki67 (1:500, Abcam), Rabbit anti-
623 PIEZO1 (1:100, Proteintech). Staining intensity was evaluated in well-defined
624 reference by quantitative (immuno-) histomorphometry using NIH ImageJ
625 software.

626 **In vitro Ca^{2+} imaging**

627 HFs were incubated with Fluo-4 staining solution (Beyotime) in culture medium

628 at 37℃ for 1 hour. Afterward HFs were washed with DPBS and cultured DPBS
629 with 1mM calcium. For different treatments, MCH, ML-7, YODA1 or GsMTX4
630 was added to the culture medium for 30 min. The HFs were embedded in OCT
631 and were sectioned with a Leica cryostat. Images were taken immediately to
632 record the fluorescence intensity to indicate Ca^{2+} concentration and the
633 adjacent section was used for CD34 staining to indicate progenitor cells.

634 **Statistical analysis**

635 All data were expressed as mean±SEM and were analyzed by ANOVA or
636 Kruskall-Wallis test when more than two groups were compared or Student's t-
637 test when only two groups were compared. Graphpad Prism 8, R (v4.1.3) and
638 Excel (Microsoft) were used to assess statistical significance. Statistical
639 significance was set at a $P < 0.05$. *, ** and *** indicate $P < 0.05$, $P < 0.01$ and
640 $P < 0.001$, respectively.

641 **Data availability**

642 All data needed to assess the conclusions in the present study are provided in
643 the manuscript and/or the Supplementary Materials. The scRNA-seq datasets
644 are available from the genome sequence archive under accession number
645 HRA005629 (http://bigd.big.ac.cn/gsa-human/). Any other data supporting the
646 findings of this study are available from the corresponding author upon
647 reasonable request.

648

649 **Acknowledgements**

650 This work was supported by the National Natural Science Funds for
651 Distinguished Young Scholars (No. 82225039), the National Key Research and
652 Development Program of China (No. 2023YFC2509003), the National Natural
653 Science Foundation of China (No. 82304057, No. 81874251, No. 82073457,
654 No. 82173448, No. 82373508, No. 82303992), the Natural Science Funds of
655 Hunan province for excellent Young Scholars (No. 2023JJ20094), the Natural
656 Science Foundation of Hunan Province, China (No. 2021JJ31079). We thank
657 our colleagues (Department of Dermatology, Xiangya Hospital, Central South

University, China) for their generous support throughout this work.

Author contributions

J.L., Z.D., G.L. and L.Y. designed and conceived the study. Z.D., G.L. and L.Y. performed data analyses. L.Y. and Z.D. performed scRNA-seq analysis. G.L., Z.D., S.D. and M.C. performed most experiments. Y.Z., F.L., Y.T., Y.W., S.X., Z.W., B.W., Z.Z. and W.S. contributed to sample collection. Z.D. and M.C. help to generate sequencing libraries. H.X. and Y.Z. provide critical discussion and suggestion. Z.D., G.L., L.Y. and J.L. prepared the manuscript with input from coauthors.

Competing interests

The authors declare no competing interests.

References

1. J. M. Ceruti, G. J. Leiros, M. E. Balana, Androgens and androgen receptor action in skin and hair follicles. *Mol Cell Endocrinol* **465**, 122-133 (2018).
2. S. Inui, S. Itami, Androgen actions on the human hair follicle: perspectives. *Exp Dermatol* **22**, 168-171 (2013).
3. F. Liu *et al.*, Prediction of male-pattern baldness from genotypes. *Eur J Hum Genet* **24**, 895-902 (2016).
4. T. Katzer, A. Leite Junior, R. Beck, C. da Silva, Physiopathology and current treatments of androgenetic alopecia: Going beyond androgens and anti-androgens. *Dermatol Ther* **32**, e13059 (2019).
5. A. Adil, M. Godwin, The effectiveness of treatments for androgenetic alopecia: A systematic review and meta-analysis. *J Am Acad Dermatol* **77**, 136-141 e135 (2017).
6. Z. Deng *et al.*, Androgen Receptor-Mediated Paracrine Signaling Induces Regression of Blood Vessels in the Dermal Papilla in Androgenetic Alopecia. *J Invest Dermatol* **142**, 2088-2099 e2089 (2022).
7. Z. Deng *et al.*, mTOR signaling promotes stem cell activation via counterbalancing BMP-mediated suppression during hair regeneration. *J Mol Cell Biol* **7**, 62-72 (2015).
8. Y. Gu, Q. Bian, Y. Zhou, Q. Huang, J. Gao, Hair follicle-targeting drug delivery strategies for the management of hair follicle-associated disorders. *Asian J Pharm Sci* **17**, 333-352 (2022).
9. L. A. Garza *et al.*, Prostaglandin D2 inhibits hair growth and is elevated in bald scalp of men with androgenetic alopecia. *Sci Transl Med* **4**, 126ra134 (2012).
10. M. V. Plikus, C. M. Chuong, Macroenvironmental regulation of hair cycling and collective regenerative behavior. *Cold Spring Harb Perspect Med* **4**, a015198 (2014).

695 11. B. A. Morgan, The dermal papilla: an instructive niche for epithelial stem and progenitor cells
696 in development and regeneration of the hair follicle. *Cold Spring Harb Perspect Med* **4**, a015180
697 (2014).
698 12. N. Heitman *et al.*, Dermal sheath contraction powers stem cell niche relocation during hair
699 cycle regression. *Science* **367**, 161-166 (2020).
700 13. E. Festa *et al.*, Adipocyte lineage cells contribute to the skin stem cell niche to drive hair cycling.
701 *Cell* **146**, 761-771 (2011).
702 14. L. A. Garza *et al.*, Bald scalp in men with androgenetic alopecia retains hair follicle stem cells
703 but lacks CD200-rich and CD34-positive hair follicle progenitor cells. *J Clin Invest* **121**, 613-622
704 (2011).
705 15. F. Lolli *et al.*, Androgenetic alopecia: a review. *Endocrine* **57**, 9-17 (2017).
706 16. S. Ntshingila, N. P. Khumalo, M. Engel, A. T. Arowolo, An appraisal of laboratory models of
707 androgenetic alopecia: A systematic review. *Skin Health Dis* **1**, e15 (2021).
708 17. A. Deutsch, B. N. McLellan, K. Shinoda, Single-cell transcriptomics in dermatology. *JAAD Int* **1**,
709 182-188 (2020).
710 18. E. Mereu *et al.*, Benchmarking single-cell RNA-sequencing protocols for cell atlas projects. *Nat*
711 *Biotechnol* **38**, 747-755 (2020).
712 19. E. Papalexi, R. Satija, Single-cell RNA sequencing to explore immune cell heterogeneity. *Nat Rev*
713 *Immunol* **18**, 35-45 (2018).
714 20. S. S. Potter, Single-cell RNA sequencing for the study of development, physiology and disease.
715 *Nat Rev Nephrol* **14**, 479-492 (2018).
716 21. S. Jin *et al.*, Inference and analysis of cell-cell communication using CellChat. *Nat Commun* **12**,
717 1088 (2021).
718 22. J. W. Oh *et al.*, A Guide to Studying Human Hair Follicle Cycling In Vivo. *J Invest Dermatol* **136**,
719 34-44 (2016).
720 23. E. A. Langan, M. P. Philpott, J. E. Kloepper, R. Paus, Human hair follicle organ culture: theory,
721 application and perspectives. *Exp Dermatol* **24**, 903-911 (2015).
722 24. Z. Zou *et al.*, A Single-Cell Transcriptomic Atlas of Human Skin Aging. *Dev Cell* **56**, 383-397 e388
723 (2021).
724 25. R. Takahashi *et al.*, Defining Transcriptional Signatures of Human Hair Follicle Cell States. *J*
725 *Invest Dermatol* **140**, 764-773 e764 (2020).
726 26. S. Wu *et al.*, Single-cell transcriptomics reveals lineage trajectory of human scalp hair follicle
727 and informs mechanisms of hair graying. *Cell Discov* **8**, 49 (2022).
728 27. H. He *et al.*, Single-cell transcriptome analysis of human skin identifies novel fibroblast
729 subpopulation and enrichment of immune subsets in atopic dermatitis. *J Allergy Clin Immunol*
730 **145**, 1615-1628 (2020).
731 28. S. Joost *et al.*, Single-Cell Transcriptomics of Traced Epidermal and Hair Follicle Stem Cells
732 Reveals Rapid Adaptations during Wound Healing. *Cell Rep* **25**, 585-597 e587 (2018).
733 29. W. Rahmani *et al.*, Hair follicle dermal stem cells regenerate the dermal sheath, repopulate the
734 dermal papilla, and modulate hair type. *Dev Cell* **31**, 543-558 (2014).
735 30. S. Joost *et al.*, The Molecular Anatomy of Mouse Skin during Hair Growth and Rest. *Cell Stem*
736 *Cell* **26**, 441-457 e447 (2020).
737 31. X. Liu *et al.*, Single-Cell RNA-Sequencing Reveals Lineage-Specific Regulatory Changes of
738 Fibroblasts and Vascular Endothelial Cells in Keloids. *J Invest Dermatol* **142**, 124-135 e111

739 (2022).
740 32. T. K. Hughes *et al.*, Second-Strand Synthesis-Based Massively Parallel scRNA-Seq Reveals
741 Cellular States and Molecular Features of Human Inflammatory Skin Pathologies. *Immunity* **53**,
742 878-894 e877 (2020).
743 33. C. Y. Cui, D. Schlessinger, Eccrine sweat gland development and sweat secretion. *Exp Dermatol*
744 **24**, 644-650 (2015).
745 34. S. Joost *et al.*, Single-Cell Transcriptomics Reveals that Differentiation and Spatial Signatures
746 Shape Epidermal and Hair Follicle Heterogeneity. *Cell Syst* **3**, 221-237 e229 (2016).
747 35. H. Yang, R. C. Adam, Y. Ge, Z. L. Hua, E. Fuchs, Epithelial-Mesenchymal Micro-niches Govern
748 Stem Cell Lineage Choices. *Cell* **169**, 483-496 e413 (2017).
749 36. J. Cao *et al.*, The single-cell transcriptional landscape of mammalian organogenesis. *Nature* **566**,
750 496-502 (2019).
751 37. P. A. Martino, N. Heitman, M. Rendl, The dermal sheath: An emerging component of the hair
752 follicle stem cell niche. *Exp Dermatol* **30**, 512-521 (2021).
753 38. H. Matsumura *et al.*, Hair follicle aging is driven by transepidermal elimination of stem cells via
754 COL17A1 proteolysis. *Science* **351**, aad4395 (2016).
755 39. H. Morinaga *et al.*, Obesity accelerates hair thinning by stem cell-centric converging
756 mechanisms. *Nature* **595**, 266-271 (2021).
757 40. A. Nayak *et al.*, Single-molecule analysis reveals that regulatory light chains fine-tune skeletal
758 myosin II function. *J Biol Chem* **295**, 7046-7059 (2020).
759 41. F. Huang *et al.*, Calcium-activated chloride channel TMEM16A modulates mucin secretion and
760 airway smooth muscle contraction. *Proc Natl Acad Sci U S A* **109**, 16354-16359 (2012).
761 42. M. Kudo *et al.*, IL-17A produced by alphabeta T cells drives airway hyper-responsiveness in
762 mice and enhances mouse and human airway smooth muscle contraction. *Nat Med* **18**, 547-
763 554 (2012).
764 43. G. S. Lynch, J. G. Ryall, Role of beta-adrenoceptor signaling in skeletal muscle: implications for
765 muscle wasting and disease. *Physiol Rev* **88**, 729-767 (2008).
766 44. S. P. Cairns, F. Borrani, beta-Adrenergic modulation of skeletal muscle contraction: key role of
767 excitation-contraction coupling. *J Physiol* **593**, 4713-4727 (2015).
768 45. J. Colgren, S. A. Nichols, MRTF specifies a muscle-like contractile module in Porifera. *Nat*
769 *Commun* **13**, 4134 (2022).
770 46. X. Li *et al.*, The Caspase Inhibitor Z-VAD-FMK Alleviates Endotoxic Shock via Inducing
771 Macrophages Necroptosis and Promoting MDSCs-Mediated Inhibition of Macrophages
772 Activation. *Front Immunol* **10**, 1824 (2019).
773 47. Y. Xie *et al.*, Hair shaft miniaturization causes stem cell depletion through mechanosensory
774 signals mediated by a Piezo1-calcium-TNF-alpha axis. *Cell Stem Cell* **29**, 70-85 e76 (2022).
775 48. J. M. Kefauver, A. B. Ward, A. Patapoutian, Discoveries in structure and physiology of
776 mechanically activated ion channels. *Nature* **587**, 567-576 (2020).
777 49. S. S. Ranade, R. Syeda, A. Patapoutian, Mechanically Activated Ion Channels. *Neuron* **87**, 1162-
778 1179 (2015).
779 50. R. R. Driskell, C. Clavel, M. Rendl, F. M. Watt, Hair follicle dermal papilla cells at a glance. *J Cell*
780 *Sci* **124**, 1179-1182 (2011).
781 51. C. L. Chen, W. Y. Huang, E. H. C. Wang, K. Y. Tai, S. J. Lin, Functional complexity of hair follicle
782 stem cell niche and therapeutic targeting of niche dysfunction for hair regeneration. *J Biomed*

Sci **27**, 43 (2020).
52. J. L. Martel, J. H. Miao, T. Badri, in *StatPearls*. (Treasure Island (FL), 2023).
53. M. V. Plikus, New activators and inhibitors in the hair cycle clock: targeting stem cells' state of competence. *J Invest Dermatol* **132**, 1321-1324 (2012).
54. C. Jaworsky, A. M. Kligman, G. F. Murphy, Characterization of inflammatory infiltrates in male pattern alopecia: implications for pathogenesis. *Br J Dermatol* **127**, 239-246 (1992).
55. N. Peyravian, S. Deo, S. Daunert, J. J. Jimenez, The Inflammatory Aspect of Male and Female Pattern Hair Loss. *J Inflamm Res* **13**, 879-881 (2020).
56. C. M. Magro, A. Rossi, J. Poe, S. Manhas-Bhutani, N. Sadick, The role of inflammation and immunity in the pathogenesis of androgenetic alopecia. *J Drugs Dermatol* **10**, 1404-1411 (2011).
57. L. Martinez-Jacobo, C. D. Villarreal-Villarreal, R. Ortiz-Lopez, J. Ocampo-Candiani, A. Rojas-Martinez, Genetic and molecular aspects of androgenetic alopecia. *Indian J Dermatol Venereol Leprol* **84**, 263-268 (2018).
58. P. Martino *et al.*, Progenitor-derived endothelin controls dermal sheath contraction for hair follicle regression. *Nat Cell Biol* **25**, 222-234 (2023).
59. Y. Hao *et al.*, Integrated analysis of multimodal single-cell data. *Cell* **184**, 3573-3587 e3529 (2021).
60. G. La Manno *et al.*, RNA velocity of single cells. *Nature* **560**, 494-498 (2018).
61. D. H. Bechhofer, J. A. Kornacki, W. Firshein, D. H. Figurski, Gene control in broad host range plasmid RK2: expression, polypeptide product, and multiple regulatory functions of korB. *Proc Natl Acad Sci U S A* **83**, 394-398 (1986).
62. X. Qiu *et al.*, Reversed graph embedding resolves complex single-cell trajectories. *Nat Methods* **14**, 979-982 (2017).
63. Z. Deng *et al.*, A positive feedback loop between mTORC1 and cathelicidin promotes skin inflammation in rosacea. *EMBO Mol Med* **13**, e13560 (2021).

Figures and Figure legends

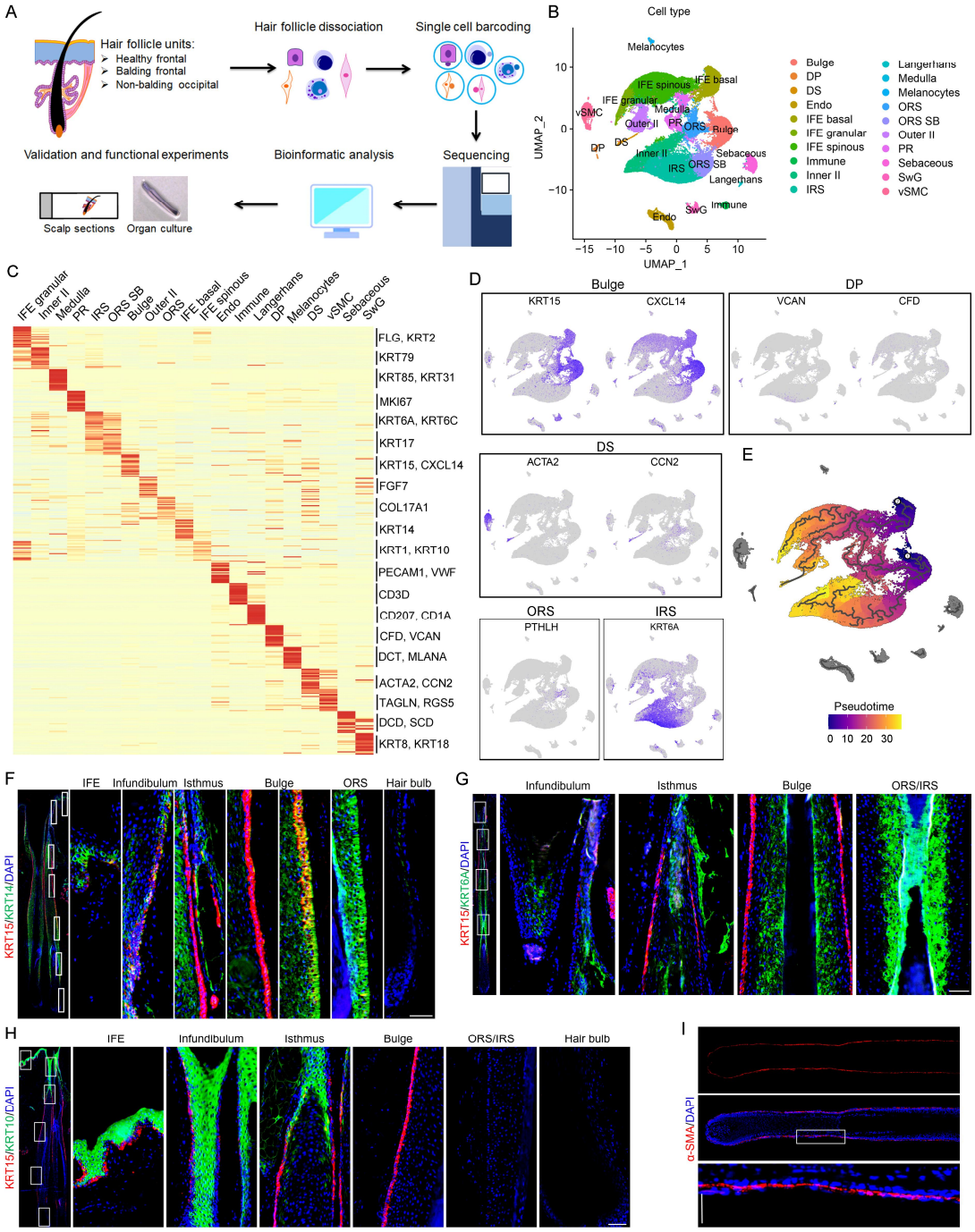

Fig. 1: scRNA-seq reveals cell type composition in anagen HF units of AGA and healthy scalps.

A Flowchart overview of scRNA-seq, and subsequent validation and functional experiments with anagen HFs from balding frontal and non-balding occipital scalps of AGA patients, and normal scalps of healthy individuals. **B** Uniform manifold approximation and projection (UMAP) plot showing the twenty cell

829 types of human anagen HFs. DP, dermal papilla; DS, dermal sheath; Endo,
830 endothelial cells; IFE, interfollicular epidermis; Inner II, inner layer of
831 infundibulum and isthmus; IRS, inner root sheath; ORS, outer root sheath basal;
832 ORS SB, outer root sheath suprabasal; Outer II, outer layer of infundibulum and
833 isthmus; PR, proliferating progenitors; SwG, sweat gland; vSMC, vascular
834 smooth muscle cells. **C** Heatmap of top 20 marker genes of each HF cell type.
835 **D** Feature plots showing expression of marker genes for the Bulge (KRT15,
836 KRT14), DP (VCAN, CFD), DS (ACTA2, CCN2), ORS (PTHLH), IRS (KRT6A).
837 **E** Monocle3 pseudotime of all HF cell types. **F-I** Representative immunostaining
838 images of KRT15/KRT14 (**F**), KRT6A/KRT15 (**G**), KRT15/KRT10 (**H**) and α-
839 SMA (**I**) in human scalp sections and the corresponding magnified views of
840 boxed areas. (n=5 HFs from 3 individuals. The same 3 individuals' samples
841 were used in all following stainings unless otherwise noted). Scale bar: 50 μm.

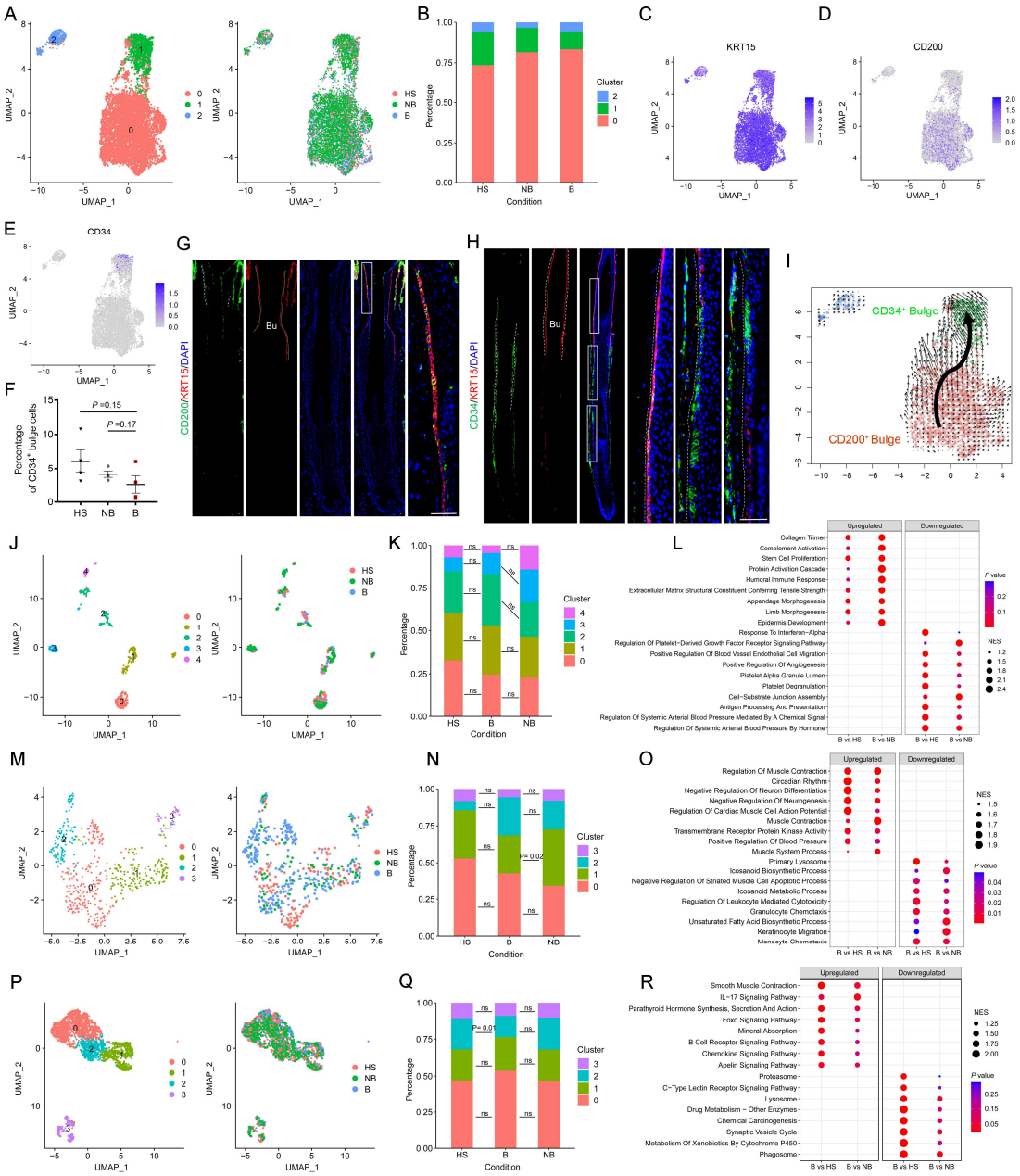

Fig. 2: Heterogeneity of cell subpopulations in AGA and healthy scalps. **A** UMAP plots showing subclusters and sample conditions of bulge cells. **B** Bar graph representing the percentage of subpopulations of bulge cells. **C-E** Feature plots showing the expression of the KRT15 (**C**), CD200 (**D**) and CD34 (**E**) in bulge cells. **F** The ratio of CD34^{+} bulge cells in Healthy (HS), non-balding (NB) and balding (B) conditions. **G, H** Representative images showing CD200 protein expression in upper bulge stem cells (**G**) and CD34 in progenitor cells (**H**). Right panels, magnified images of boxed areas. Bu, bulge. Red, KRT15 (K15) staining. DAPI staining (blue) indicates nuclear localization. ORS–DS

852 boundary is indicated by dashed lines. Scale bar: 50 μm. **I** velocyto showing
853 the single-cell trajectories of bulge subclusters in UMAP. **J** UMAP plots showing
854 subclusters and sample conditions of DP cells. **K** Bar graph representing the
855 percentage of subpopulations of DP cells. **L** Representative GO terms of
856 upregulated (left) and downregulated (right) DEGs between balding and healthy
857 groups (B vs HS), balding and non-balding groups (B vs NB) in DP cells. NES
858 stands for enrichment scores. The color keys from red to blue indicate the range
859 of P value. **M** UMAP plot showing subclusters and sample conditions of DS
860 cells. **N** Bar graph representing the percentage of subpopulations of DS cells.
861 **O** Representative GO terms enriched in balding versus non-balding or healthy
862 DS cells. NES stands for enrichment scores. The color keys from red to blue
863 indicate the range of p value. e. **P** UMAP plot showing subclusters and sample
864 conditions of vSMC cells. **Q** Bar graph representing the percentage of
865 subpopulations of vSMC cells. **R** Representative GO terms enriched in balding
866 versus non-balding or healthy vSMC cells. NES stands for enrichment scores.
867 The color keys from red to blue indicate the range of p value. The data represent
868 the means±SEM. P values were determined by unpaired (B vs HS) or paired (B
869 vs NB) student's t-test. ns, not significant.

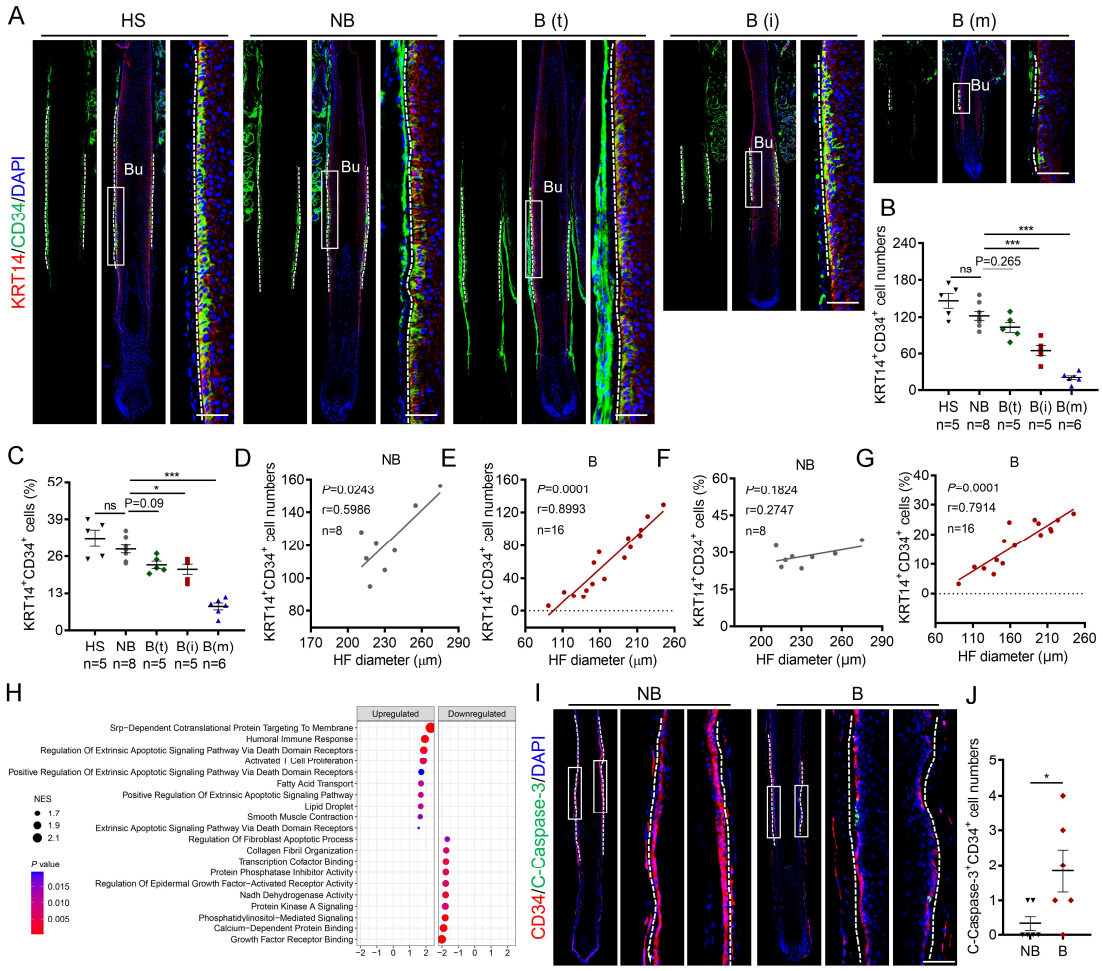

Fig. 3: Apoptotic loss of HF progenitor cells is associated with HF miniaturization in AGA.

A Immunostaining images show progenitor cells in HS terminal HFs (n=5 anagen HFs from 3 individuals), NB terminal HFs (n=8 anagen HFs) and B terminal /intermediate /mini HFs (B(t)/B(i)/B(m), n=5/5/6 anagen HFs) from 3 AGA patients. Epidermal cells and progenitor cells were labelled with KRT14 (red) and CD34 (green) respectively and ORS–DS boundary is indicated by dashed lines. Right panels, magnified images of boxed areas. Bu, bulge. Types of HFs were defined by their diameter. Terminal: diameter>200 μm; Intermediate: 150 μm <diameter<200 μm; mini: diameter<150 μm. **B, C** Quantification of the number of KRT14$^+$CD34$^+$ progenitor cells in different groups (**B**) and their proportion in the total outer layer of HFs (**C**). **D-G** Scatter plots show the correlation between HF diameters and the number or percentage of KRT14$^+$CD34$^+$ progenitor cells in AGA patients. Spearman's

885 correlation coefficient was used for the correlation analysis (two-tailed). **H**
886 Top10 GO terms upregulated or downregulated in B versus in NB $CD34^+$
887 progenitor cells. NES stands for enrichment scores. The color keys from red to
888 blue indicate the range of P value. **I, J** Representative images of C-Caspase-3
889 and CD34 co-immunostaining on anagen HFs from NB and B scalps of AGA
890 patients (n=6 HFs from 3 donors for each group); Right panels, magnified
891 images of boxed areas (**I**). The quantification of C-Caspase-3^+CD34^+ cell
892 numbers in two groups (**J**). Progenitor cells were indicated with dotted line.
893 Scale bar: 50μm. The data represent the means±SEM. *P<0.05, **P<0.01,
894 ***P<0.001, determined by one-way ANOVA with Tukey's post hoc test (**B, C**)
895 or unpaired Student's t-test (**J**). ns, not significant.

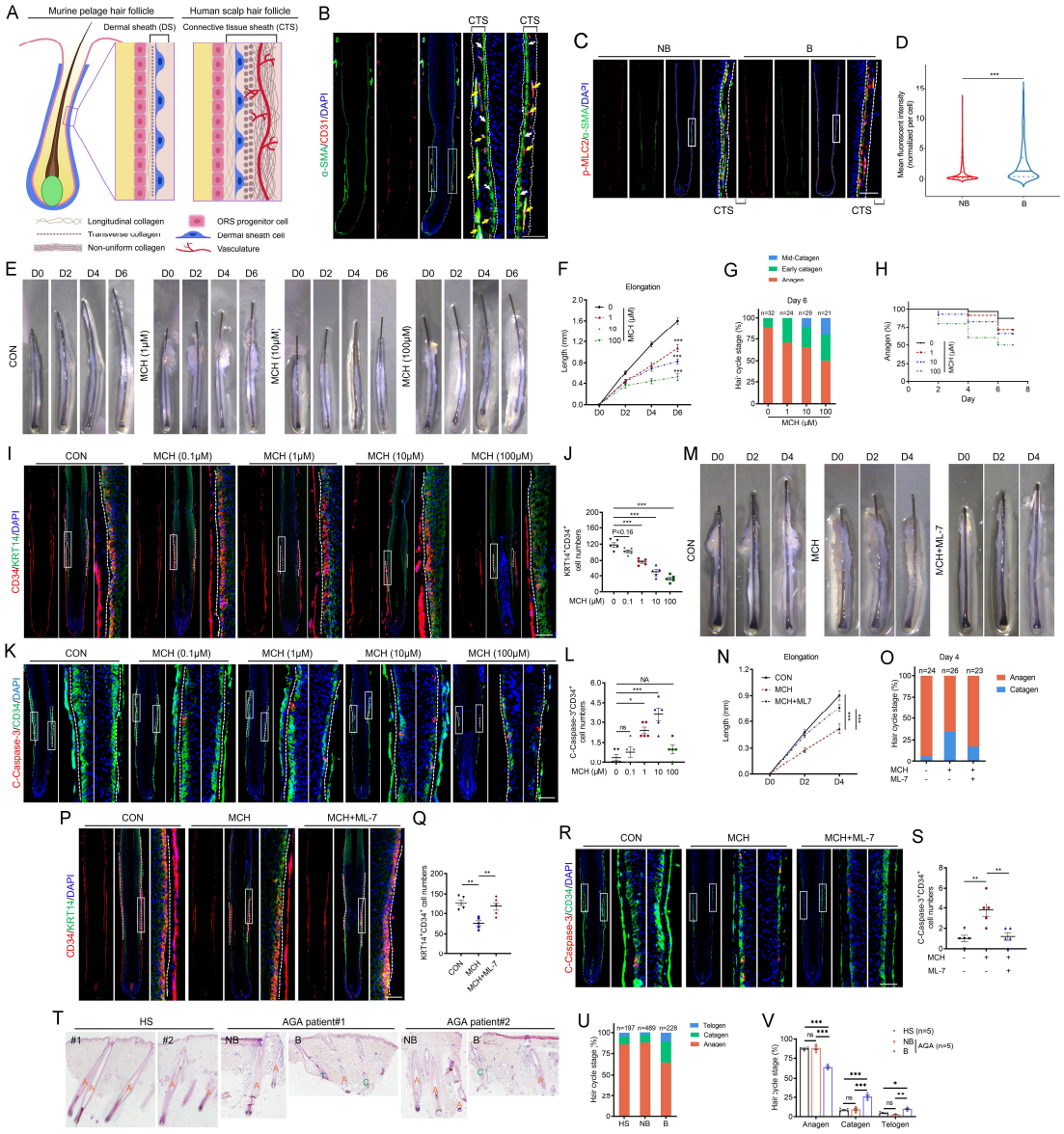

Fig. 4: Hyperactive CTS contraction induces premature hair regression in AGA.

A Dermal sheath (DS)/ connective tissue sheath (CTS) in murine pelage follicle/ human scalp follicle. This image is adapted from the previous publication (*37*). In murine pelage follicle (left), the DS is the outer layer of the ORS progenitors. In human scalp follicle, the outer layer is the CTS (right), which is mainly composed of DS cells, vasculature and multiple types of collagens. **B** Immunostaining of CD31 (an endothelial cell marker) and α-SMA (a marker for both DS and vSMC cells) in human scalps with anagen HFs. CTS is located between the two dotted lines. White arrows indicate DS. Yellow arrows indicate

907 blood vessels. Right panels, magnified images of boxed areas. **C** The activation
908 of CTS contraction was evaluated with p-MLC2 immunostaining on anagen HFs
909 from non-balding occipital scalps (n=5 HFs) and balding frontal scalps (n=6 HFs)
910 of 3 AGA patients. Right panels, magnified images of boxed areas. **D**
911 Quantification of relative mean fluorescent intensity (RFI) of p-MLC2 in α-SMA
912 positive cells in CTS in different groups. **E** Representative images of hair shaft
913 elongation of human HFs ex vivo with vehicle (CON) or MCH treatment at
914 concentration of 0.1 μM, 1 μM, 10 μM, 100 μM as indicated (n=21-32 HFs from
915 3 donors for each group). The same individuals' HF samples were used in the
916 following staining of HFs with the same treatments. **F** Quantification of hair shaft
917 elongation on day 2/4/6 with indicated treatments (n=32/24/29/21 in different
918 groups respectively). **G** Macroscopic quantification of hair cycle stage of HFs
919 with vehicle or MCH treatments on day 6. **H** Percentages of HFs in anagen on
920 day 2/4/6 with indicated treatments. **I** Representative images of co-
921 immunostaining of CD34 and KRT14 in HFs with vehicle or MCH treatments on
922 day 4. **J** Quantification of $KRT14^{+}CD34^{+}$ progenitor cell numbers in the total
923 outer layer of HFs. **K** Apoptosis of progenitor cells were indicated with co-
924 immunostaining of CD34 and C-Caspase-3 on day 2. Progenitor cells were
925 indicated with and located inside the dotted lines. Right panels, magnified
926 images of boxed areas. **L** Quantification of C-Caspase-$3^{+}CD34^{+}$ progenitor
927 cells in HFs. To be mentioned, C-Caspase-$3^{+}CD34^{+}$ progenitor cells are barely
928 detectable under 100 μM MCH administration because CD34+ progenitor cells
929 were almost vanished under this condition. **M** Representative images of hair
930 shaft elongation of human HFs ex vivo with vehicle or MCH (10 μM) and ML-7
931 (0.3 μM) treatment as indicated (n=23-26 HFs from 3 donors for each group,
932 independent experiments). **N** Quantification of hair shaft elongation on day 2/4
933 with vehicle or MCH and ML-7 treatments (n=24/26/23 in different groups
934 respectively). **O** Macroscopic quantification of hair cycle stage of HFs with
935 vehicle or MCH and ML-7 treatments on day 4. **P** Co-immunostaining of CD34
936 and KRT14 on day 4. Right panels, magnified images of boxed areas. **Q**

937 Quantification of total KRT14^{+}CD34^{+} progenitor cell numbers in HFs (n=5 HFs
938 from 3 donors for each group). **R** Co-immunostaining of CD34 and C-Caspase-
939 3 showed progenitor cell apoptosis with indicated treatments on day 2 (n=5 HFs
940 from 3 donors for each group). Right panels, magnified images of boxed areas.
941 **S** Quantification of C-Caspase-3^{+}CD34^{+} progenitor cells numbers in HFs (n=5
942 HFs from 3 donors for each group). **T** Representative images of HE staining
943 with HS frontal scalps, NB occipital and B frontal scalps from AGA patients. A,
944 anagen HF. C, catagen HF. T, telogen HF. **U** Macroscopic quantification of hair
945 cycle stage of HFs in HE staining (n=197/489/228 HFs from 5 HS and 5 AGA
946 donors). **V** Percentage of anagen, catagen and telogen HFs in HS, NB and B
947 scalps (n=197/489/228 HFs from 5 HS and 5 AGA donors). Scale bar, 50 μm.
948 Data are expressed as mean±SEM and were analyzed by one-way ANOVA with
949 Tukey's post hoc test (J, L, Q, S, V) and two-way ANOVA with a post hoc Holm–
950 Sidak's multiple comparisons test (F, N), or unpaired Student's t-test (D).
951 *p<0.05, **p<0.01, ***p<0.001. ns, not significant. NA, not applicable.

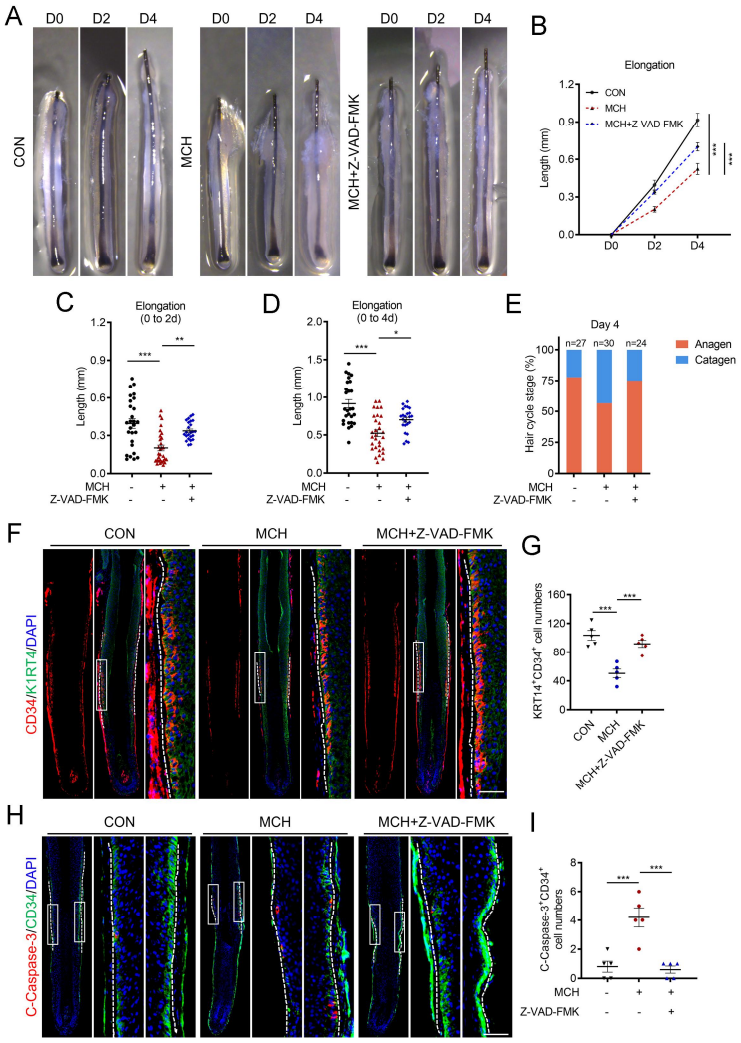

Fig. 5: CTS contraction drives premature hair regression in an apoptosis-dependent manner.

A Representative images of hair shaft elongation of human HFs ex vivo with or without MCH (10 μM) and Z-VAD-FMK (10 μM) as indicated (n=24-30 anagen HFs from 3 donors for each group). The same individuals' HF samples were used in the following staining of HFs with the same treatments. **B** Quantification of hair shaft elongation on day 2/4/6 with indicated treatments. **C, D** Scatter plots show the elongation length of hair shaft with indicated treatments on day 2 (**C**) and day 4 (**D**). **E** Macroscopic quantification of hair cycle stage of HFs with indicated treatments on day 4. **F** Co-immunostaining of CD34 and KRT14 on day 4. Right panels, magnified images of boxed areas. **G** Quantification of total $KRT14^{+}CD34^{+}$ progenitor cell numbers in HFs with indicated treatments

965 (n=5 HFs for each group). **H** Co-immunostaining of CD34 and C-Caspase-3
966 showed apoptosis of progenitor cells with indicated treatments on day 2 (n=5
967 HFs for each group). **I** Quantification of C-Caspase-3^{+}CD34^{+} progenitor cell
968 numbers in HFs with indicated treatments. Progenitor cells were indicated with
969 dotted line. Right panels, magnified images of boxed areas. Scale bar: 50 μm.
970 The data represent the means±SEM. *$p<0.05$, **$p<0.01$, ***$p<0.001$,
971 determined by one-way ANOVA with Tukey's post hoc test (C, D, G, I) and two-
972 way ANOVA with a post hoc Holm–Sidak's multiple comparisons test (B).
973
974

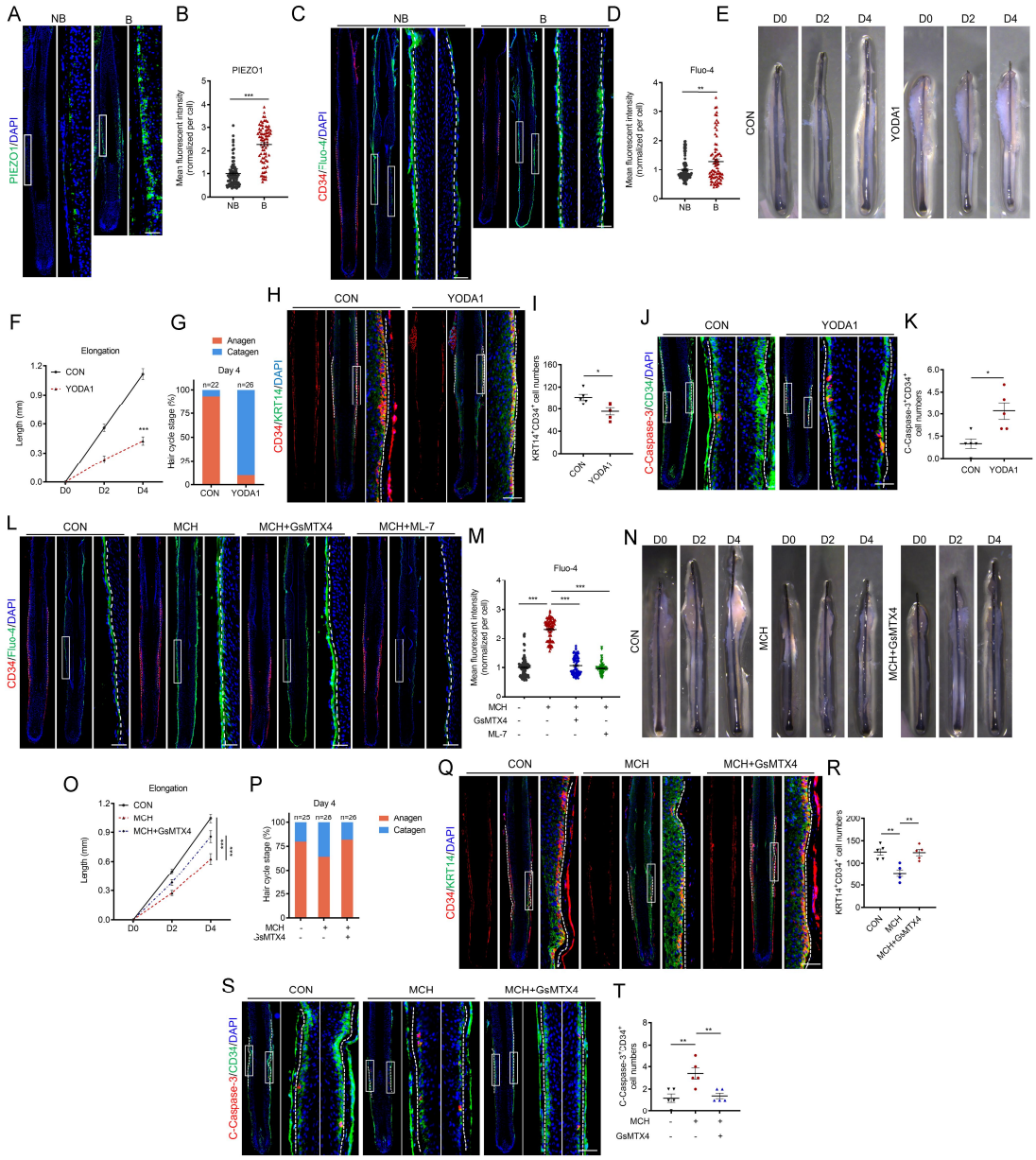

Fig. 6: PIEZO1 signaling is necessary for CTS contraction-induced progenitor cell apoptosis and premature hair regression.

A, B (**A**) Representative immunostaining of PIEZO1 on skin sections from balding frontal and non-balding occipital scalps of AGA patients (n=3) and (**B**) the quantification of mean fluorescent intensity in outermost layer of mid-HF cells (n=70-90 cells from 3 patients). **C, D** (**C**) CD34 and Fluo-4 staining were performed on serial sections from balding frontal and non-balding occipital scalps of AGA patients (n=3) and (**D**) the Fluo-4 mean fluorescent intensity in $CD34^{+}$ progenitor cells was quantified (n=100 cells in non-balding HFs and 80 cells in balding HFs from 3 patients). Fluo-4 indicates the cellular Ca^{2+}

concentration. **E** Representative images of hair shaft elongation of human HFs ex vivo with or without YODA1 (15 μM) as indicated (n=22-26 anagen HFs from 3 individuals for each group). The same individuals' HF samples were used in the following staining of HFs with the same treatments. **F** Quantification of hair shaft elongation on day 2/4 with vehicle or YODA1 treatments. **G** Macroscopic quantification of hair cycle stage of HFs with YODA1 treatment on day 4. **H** Co-immunostaining of CD34 and KRT14 on day 4. **I** Quantification of total $KRT14^{+}CD34^{+}$ progenitor cell numbers (n=5). **J** Co-immunostaining of CD34 and C-Caspase-3 showed apoptosis of progenitor cells on day 2. **K** Quantification of C-Caspase-$3^{+}CD34^{+}$ apoptotic progenitor cell numbers in HFs (n=5). **L, M** (**L**) CD34 and Fluo-4 staining were performed on serial sections of HFs with indicated treatments (n=3 HFs for each group) and (**M**) the Fluo-4 mean fluorescent intensity in $CD34^{+}$ progenitor cells was quantified (n=80-100 cells from 3 different HFs). **N** Representative images of hair shaft elongation of human anagen HFs ex vivo treated with MCH (10 μM) and GsMTX4(1 μM) (n=25 HFs for CON, 28 HFs for MCH and 26 HFs for MCH+GsMTX4; from 3 individuals). The same individuals' HF samples were used in the following staining of HFs with the same treatments. **O** Quantification of hair shaft elongation on day 2/4 with MCH and GsMTX4 treatments. **P** Macroscopic quantification of hair cycle stage of HFs with MCH and GsMTX4 treatments on day 4. **Q** Co-immunostaining of CD34 and KRT14 on day 4. **R** Quantification of total $KRT14^{+}CD34^{+}$ progenitor cell numbers in HFs (n=5 for each group). **S** Co-immunostaining of CD34 and C-Caspase-3 showed apoptosis of progenitor cells on day 2. **T** Quantification of C-Caspase-$3^{+}CD34^{+}$ progenitor cell numbers in HFs (n=5 for each group). Right panels, magnified images of boxed areas. Scale bar: 50 μm. Data are expressed as mean±SEM and were analyzed by one-way ANOVA with Tukey's post hoc test (M, R, T), two-way ANOVA with a post hoc Holm–Sidak's multiple comparisons test (F, O), and two-tailed unpaired Student's t-test (B, D, I, K). *$p<0.05$, **$p<0.01$, ***$p<0.001$.

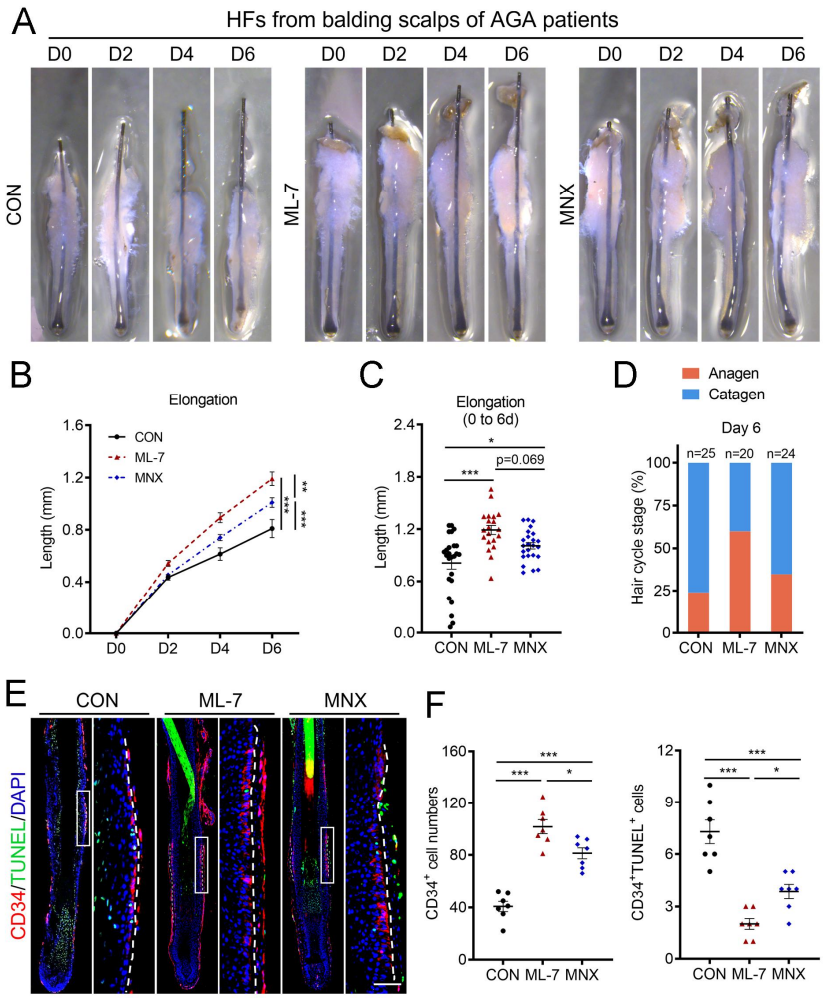

Fig. 7: ML-7 exhibits a better effect than MNX on promoting the growth of HFs from the balding scalps of AGA patients.

A Representative images of hair shaft elongation of anagen HFs from balding scalps of AGA patients ex vivo treated with vehicle (CON), ML-7 (0.3 μM) or minoxidil (MNX) ((100 μM)) as indicated (n=31-37 balding HFs from 5 AGA patients for each group). 3 patients' HF samples were used in the following staining. **B** Quantification of hair shaft elongation on day 2/4/6 with indicated treatments. **C** Scatter plots show the elongation length of hair shaft on day 6. **D** Macroscopic quantification of hair cycle stage of HFs with indicated treatments on day 6. **E** Co-immunostaining of CD34 and TUNEL showed apoptosis of progenitor cells with indicated treatments (n=7 balding HFs from 3 AGA patients for each group). Right panels, magnified images of boxed areas. **F** Quantification of total and apoptosis $CD34^+$ progenitor cell numbers in HFs with

1030 indicated treatments. Scale bar: 50 μm. The data represent the means±SEM.
1031 *p<0.05, **p<0.01, ***p<0.001, determined by one-way ANOVA with Tukey's
1032 post hoc test (C, F) and two-way ANOVA with a post hoc Holm–Sidak's multiple
1033 comparisons test (B).
1034